Check for updates

ADVANCED ENGINEERING MATERIALS
www.aem-journal.com

Experimental and Numerical Modal Characterization for Additively Manufactured Triply Periodic Minimal Surface Lattice Structures: Comparison between Free-Size and Homogenization-Based Optimization Methods

*Mirhan Ozdemir, Ugur Simsek, Engin Kuser, Cemal Efe Gayir, Alican Celik, and Polat Sendur**

Homogenization-based topology optimization (HMTO) is one of the most extensively used grading methods to generate functionally graded lattice structures (FGLs). However, it requires a precharacterization of the lattices, which is time-consuming. As a remedy, free-size optimization-based graded lattice generation (FOGLG) is explored as an alternative method to generate the FGLs. This article builds on the authors' previous work in which the HMTO and FOGLG approaches are studied to improve the dynamic characteristic of a design by using a single lattice type, namely, double gyroid (DG) structure. To show applicability of the proposed methods, different lattice types including diamond (D), gyroid (G), and I-WP are employed to create FGLs herein. The frequency response analysis is performed, and the results from HMTO and FOGLG are compared in terms of their accuracy and efficiency. The optimized designs are then reconstructed by relative density mapping (RDM) and enhanced relative density mapping (ERDM) methods. The fabricated test samples made of cobalt–chromium using the direct metal laser melting (DMLM) technique are then experimentally validated using a laser vibrometer. The results reveal that HMTO and FOGLG can be used on the lattice types with a variety of configurations and relative densities.

1. Introduction

Additive manufacturing (AM), a substantial breakthrough over traditional manufacturing processes, has evolved significantly over the last few decades to meet industry demand.[1,2] It enables designers to utilize nature-inspired complex structures such as triply periodic minimal surface (TPMS) lattice structures.[3–5] The TPMS structures are desired and topologically ordered in many design applications due to their attractive properties, such as being lightweight and enhanced mechanical properties.[6,7] Another advantage of these structures is that their mechanical performance and functionality can be further improved by altering the thickness of given structures.[8–10]

The quest for the ideal structure prompts new optimization proposals in the literature. Topology optimization (TO), which defines the best material distribution within the design domain, is one of the most extensively utilized optimization methods in the literature.[11–13] Among the various mathematical methods for TO, the solid isotropic material with penalization (SIMP), proposed by Rozvany et al.,[14] gained significant attention due to its simplicity in implementation for the TO. The application of this approach to generate multiclass microstructures made of truss elements is available in the literature. For example, surrogate models for different truss-based structures are used in TO to minimize the compliance of the structure for a given volume ratio. The methodology was demonstrated on 2D and 3D case studies.[15] In another study,[16]

M. Ozdemir, E. Kuser, P. Sendur
Mechanical Engineering Department
Ozyegin University
34794 Istanbul, Turkey
E-mail: polat.sendur@ozyegin.edu.tr

The ORCID identification number(s) for the author(s) of this article can be found under https://doi.org/10.1002/adem.202201811.

© 2023 The Authors. Advanced Engineering Materials published by Wiley-VCH GmbH. This is an open access article under the terms of the Creative Commons Attribution-NonCommercial-NoDerivs License, which permits use and distribution in any medium, provided the original work is properly cited, the use is non-commercial and no modifications or adaptations are made.

DOI: 10.1002/adem.202201811

M. Ozdemir, C. E. Gayir, P. Sendur
Vibrations and Acoustics Laboratory
Ozyegin University
34794 Istanbul, Turkey

U. Simsek, A. Celik
Additive Manufacturing
TTC – General Electric (GE) Marmara Technology Center
41471 Kocaeli, Turkey

15272648, 2023, 11, Downloaded from https://onlinelibrary.wiley.com/doi/10.1002/adem.202201811 by Ozyegin University, Wiley Online Library on [06/09/2023]. See the Terms and Conditions (https://onlinelibrary.wiley.com/terms-and-conditions) on Wiley Online Library for rules of use; OA articles are governed by the applicable Creative Commons License

eight different types of unit cells are optimized using a design parameterization algorithm, where each phase is modeled using beam elements. However, the resulting structure becomes stiffer due to node-to-node connection. In a more recent study,[17] the topology optimization uses Kriging-based models to generate a functionally graded lattice sandwich structure consisting of body-centered cubic lattices. The thickness of the face sheets and the density of the lattice cells in the core structure are optimized to minimize the compliance and maximize the first natural frequency for a given volume constraint. In a similar study, Gao et al.[18] proposed a concurrent TO for multiscale structures. They used a modified SIMP-based TO method to develop a compact and efficient MATLAB script for TO of 2D and 3D designs infilled with lattice structures. Liu et al.[19] adopted TO to obtain a graded lattice design by moving the morphable components/voids (MMC/MMV). The application of TO for grading TPMS structures is also vast in the literature. For example, functionally graded gyroid structures are obtained by integrating the material scaling law into the direction constrained FGCS optimization algorithm.[20] The density of the structure is optimized by tuning the level parameter according to the topology optimization results and the 3D printing direction. The objective is to minimize the compliance of the structure for a given volume fraction. Gyroid (G), diamond (D), primitive, and I-WP structures are used to develop graded cellular structures using neural networks, which smooth the stress concentrations and improve the computational efficiency.[21] Another widely used optimization technique for lattice structures is homogenization-based TO (HMTO), proposed by Bendsøe and Kikuchi.[22] Groen and Sigmund used this method to produce manufacturable designs with high resolution.[23] In a more recent study, Simsek et al.[24] proposed the application of the HMTO optimization with a modified SIMP method to double gyroid (DG) surface-based lattice structures. The application of this algorithm for other types of lattice structures was acknowledged as future work in that study.

Although the HMTO method has many advantages, it requires a material characterization step prior to the optimization analysis, which is a time-consuming process. As a result, researchers have recently sought unique design techniques as an alternative to the HMTO method. The shell element-based lattice modeling is a promising method that requires less preprocessing and computing time. Due to the use of fewer design variables and simpler geometry, computational performance of shell-based optimization methods is typically more effective than HMTO's. The optimization process in shell-based optimization, which solely involves adjusting the thickness of the shell, is typically faster compared to the homogenization-based topology optimization, which involves adjusting both material properties and shape. As a result, there has been a growing trend in the literature toward the implementation of shell-based lattice modeling. For example, Simsek et al.[25] revealed that the accuracy of the finite element models (FEMs) consisting of shell elements is high for lower relative densities for various TPMS structures. There are similar applications in the literature.[26,27] Yet, the use of shell element-based models to optimize lattice structures is less common. In one such study, the mechanical performance of the lattice structures was optimized by altering the thickness properties of the shell lattices uniformly.[28] To automate the selection of optimal geometrical parameters of the design domain, size optimization is utilized in truss-like lattice structures.[29] However, establishing a global optimal thickness value for every mesh element using this technique is inefficient. To eliminate this problem, a free-size optimization method, which is a special form of size optimization, can be utilized. In the free-size method, the thickness properties of each shell element can be automatically determined by the optimization algorithm. This method is employed in a variety of sheet metal constructions to improve the mechanical properties.[30–33] In the authors' previous study,[34] free-size optimization-based graded lattice generation (FOGLG) is applied successfully for the first time to surface-based DG lattice structure. The performance of the proposed method is compared with HMTO in terms of modal response to demonstrate its effectiveness. The study concludes that the FOGLG can be used as an alternative to HMTO for the generation of functionally graded lattice structures (FGLs). However, this study is only validated on DG-type lattice, and applications for different lattice types are referred to as future work. This article is an extension of authors' previous studies.[24,25,34] In this study, the design for additive manufacturing (DfAM) technique is used to determine the best material distribution in a design domain using HMTO and FOGLG methodologies for different lattice types. More specifically, HMTO and FOGLG methods are demonstrated and compared for D, G, and I-WP in this study. The optimized geometries by HMTO and FOGLG are then reconstructed with relative density mapping (RDM)[35] and enhanced relative density mapping (ERDM),[34] respectively. The reconstructed designs of HMTO and FOGLG methods made of cobalt–chromium (CoCr) alloy are manufactured with the direct metal laser melting (DMLM) method, and experimentally validated against modal testing. In this study, Hypermesh, Optistruct, and Hyperview are used as preprocessor, solver, and postprocessor, respectively.

The article is organized as follows: the geometric and mechanical relationship of the lattices is discussed in Section 2. Section 3 provides the details and implementation of HMTO and FOGLG in a case study. Also, the optimum designs are reconstructed using RDM and ERDM algorithms based on the optimal material distribution. Section 4 is reserved for the fabrication and experimental validation. Finally, the conclusions are given in Section 5.

2. Experimental Section

2.1. Theoretical Background

Lattice structures are very popular in many design applications such as aerospace, biological, and engineering due to their superior mechanical performance such as being lightweight, having high specific strength, and stiffness.[36,37] Their geometrical and mechanical features are inextricably linked. Therefore, by modifying the lattices' geometric parameters, the mechanical response of the lattice structure can be changed, and greater properties of the materials can be revealed. The Gibson–Ashby model uses mechanical and physical factors to determine various mechanical characteristics of cellular structures. This model is described by Equation (1), which is also known as the power-law formula[38,39]

 © 2023 The Authors. Advanced Engineering Materials published by Wiley-VCH GmbH

$$E^* = C(\rho^*)^n \tag{1}$$

where E^* is the relative elastic modulus and is obtained by dividing the elastic modulus of the lattice to the elastic modulus of the constitutive material (i.e., $E^* = E_{\text{latt.}}/E_s$). The relative density, ρ^*, is determined similarly (i.e., $\rho^* = \rho_{\text{latt.}}/\rho_s$). The coefficients C and n depend on the cell topologies.[40,41] Furthermore, there are three relationships for different types of cellular materials in literature: 1) $n \cong 1$ for stretching-dominated materials, 2) $n \cong 2$ for bending-dominated materials, and 3) $n \cong 3$ for stochastic foams.[42,43] The constants of the Gibson–Ashby model is determined experimentally or numerically in the literature.[44]

2.2. Design of TPMS Structures

Surface-based TPMS lattice structures such as the D, G, and I-WP types can be represented by functions of four variables, i.e., $U(x,y,z,t)$.[45,46] The t parameter, called the level set parameter, controls the offset of the thickness at the isosurface $U = 0$, which modifies the topology of lattices. These functions for D-, G-, and I-WP-type lattice structures are given in Equation (2a), (2b), and (2c) as follows[47–49]

$$\begin{aligned} U_D(x,y,z,t) = {} & (\sin(k_x x)\sin(k_y y)\sin(k_z z)) \\ & + \cos(k_x x)\sin(k_y y)\sin(k_z z) \\ & + \sin(k_x x)\cos(k_y y)\sin(k_z z) \\ & + \sin(k_x x)\sin(k_y y)\cos(k_z z)^2) - t^2 \end{aligned} \tag{2a}$$

$$\begin{aligned} U_G(x,y,z,t) = {} & (\cos(k_x x)\sin(k_y y) + \cos(k_y y)\sin(k_z z) \\ & + \cos(k_z z)\sin(k_x x))^2 - t^2 \end{aligned} \tag{2b}$$

$$\begin{aligned} U_{I-WP}(x,y,z,t) = {} & 2(\cos(k_x x)\cos(k_y y)) + \cos(k_y y)\cos(k_z z) \\ & + \cos(k_z z)\cos(k_x x) \\ & - ((\cos(2k_x x) + \cos(2k_y y) + \cos(2k_y y))^2) - t^2 \end{aligned} \tag{2c}$$

where x, y, and z refer to 3D Euclidean spatial coordinates and $k_i = (2\pi/l_i)n_i$ where $i = x, y, z$ and l_i represents the cell dimension in the given direction, respectively. The spatial relative density of the lattice structure depends on t. These parameters are unique for each lattice structure. This unique relation between t and ρ^* is obtained by varying the parameter t and calculating the corresponding ρ^*. This process is also named t to ρ^* mapping. The unique mapping for the aforementioned lattice types is shown in **Figure 1**.

The value of the relative density for D- and G-type lattices converges to unity with increasing t, showing that these lattices do not have void domains. Therefore, increasing the t value has no influence on the topology of the structure. However, for the I-WP-type lattice, this occurs at higher values of t. As a result, an upper limit is not defined for I-WP-type lattice structures in this study. The unique formula for each lattice is obtained by fitting a linear equation for a given range of t. The equations for D, G, and I-WP-type lattices are given in Equation (3a), (3b), and (3c), respectively

$$\rho^*_D(t) = 0.8244 \times t \quad 0.1 \le t \le 0.9 \tag{3a}$$

$$\rho^*_G(t) = 0.6569 \times t \quad 0.1 \le t \le 1.2 \tag{3b}$$

$$\rho^*_{I-WP}(t) = 0.2636 \times t \quad 0.1 \le t \le - \tag{3c}$$

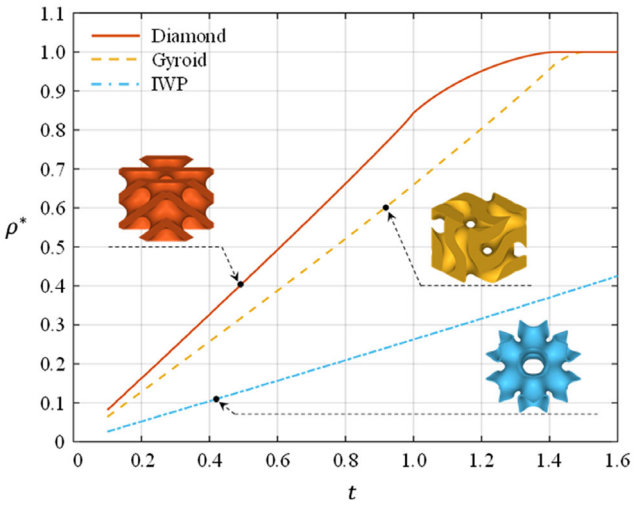

Figure 1. Relative density, ρ^*, versus level set parameter, t, for D-, G-, and I-WP-type lattices.

2.3. Frequency Response Analysis of a Sandwiched Structure as a Case Study

In this study, the dynamic performance of a functionally graded sandwiched structure made of D-, G-, and I-WP-type lattices is improved using two optimization approaches: HMTO and FOGLG. The design domain of the system is filled with $5 \times 5 \times 1$-unit cells in x, y, and z directions, respectively. The size of a unit cell is $12 \times 12 \times 12$ mm making the overall dimension of the design core is $60 \times 60 \times 12$ mm. The core is sandwiched between upper and lower plates of 0.8 mm thickness. The thickness of the plates is not included in the optimization procedure because they are regarded as nondesign domain. **Figure 2** depicts the sandwiched structure's design and nondesign domains. The mechanical properties of cobalt–chrome (CoCr) are listed in **Table 1**.[50–52] As material properties are generally affected by many factors, an average value from the literature is used in FEM.

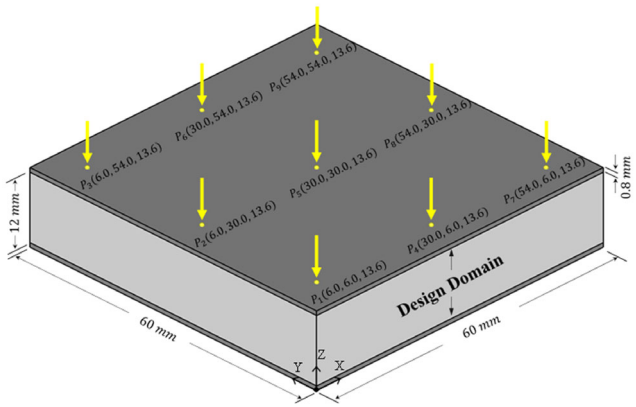

Figure 2. Schematic illustration of a sandwiched design domain.

© 2023 The Authors. Advanced Engineering Materials published by Wiley-VCH GmbH

15272648, 2023, 11, Downloaded from https://onlinelibrary.wiley.com/doi/10.1002/adem.202201811 by Ozyegin University, Wiley Online Library on [06/09/2023]. See the Terms and Conditions (https://onlinelibrary.wiley.com/terms-and-conditions) on Wiley Online Library for rules of use; OA articles are governed by the applicable Creative Commons License

Table 1. Material properties of CoCr.

Material	Elastic modulus, E_s	Poisson's ratio, ν	Density, ρ_s
CoCr	236 GPa	0.33 (−)	8.3×10^{-9} g cc^{-1}

A unit load is applied to excite the structure's first natural modes for the optimization case study of the sandwiched structure. Uniformly spaced unit loads ranging from P_1 to P_9 are applied on the plate's top surface (see Figure 2). The acceleration response is recorded at the same positions. A free-to-free boundary condition is applied to replicate the experimental setup for validation.

To understand and characterize the dynamic behavior of the solid structure, a modal analysis is carried out up to 20 kHz. The natural frequencies and mode shapes of the structure are shown in **Figure 3**. The first two natural frequencies of the solid structure are found to be 10 946 and 16 241 Hz.

As an optimization case study, the required bandgap is selected to be 20% of the first resonance frequency. Therefore, the lower and upper frequencies defining the bandgap are set to 8800 and 13 200 Hz, respectively. No resonance frequency of the structure is desired in this frequency range. The objective of the optimization algorithm is to reduce the sum of acceleration amplitude throughout the frequency range of interest. A frequency response analysis is used for this purpose. Equation (4) is used to compute the total acceleration of the structure

$$A(\omega) = \sum_{i=1}^{N} a_i(\omega) \tag{4}$$

where i and N define minimum and maximum frequencies, respectively. $A(\omega)$ is the overall acceleration, and $a_i(\omega)$ is the acceleration corresponding to the ith frequency. The root sum squares (RSS) is then used to represent the dynamic performance of the structure as a single value, as given in Equation (5)

$$\mathrm{RSS} = \sqrt{\sum_{i=6000}^{15000} A_{\mathrm{TPMS}}(\omega_i)^2} \tag{5}$$

The minimum and maximum limits of the acceleration frequency response function (FRF) are set to be 6000 and 15 000 Hz, respectively, which includes the first resonance frequency of the solid design. For this study, the target volume fraction constraint is 0.3, and the lower and higher bounds of the volume fraction are 0.1 and 0.5.

3. Optimization Approaches

The HMTO and FOGLG algorithms for the sandwiched structure infilled separately with the three lattice types are studied to improve dynamic characteristics of the sandwiched structure by varying the material distribution over the design domain. As stated before, in general, the FOGLG typically requires less computational resources than the HMTO because it deals with a smaller number of design variables and a simpler geometry. The optimization process in the FOGLG is usually faster as it only involves adjusting the thickness of the shell, whereas in the HMTO the optimization process involves adjusting both material properties and shape. However, the solution obtained from the FOGLG is limited to the adjustment of thickness and may not be able to achieve optimal performance as compared to the HMTO which have more degrees of freedom to optimize. Moreover, the HMTO uses multiscale analysis which can be computationally expensive, especially when it comes to postprocessing the results. The primary objective of this study is to enhance the dynamic performance of the design domain through the manipulation of lattice thickness. To this end, it is hypothesized that the proposed FOGLG approach will prove to be an accurate method for achieving this goal. The details of the aforementioned optimization algorithm are presented in the following sections.

3.1. HMTO

3.1.1. Elastic Modulus Determination

The HMTO requires an analytical relationship between constituent material characteristics, lattice properties, and relative density for lattice characterization. The Gibson–Ashby model (Equation (1)) was used to obtain such empirical relationship.

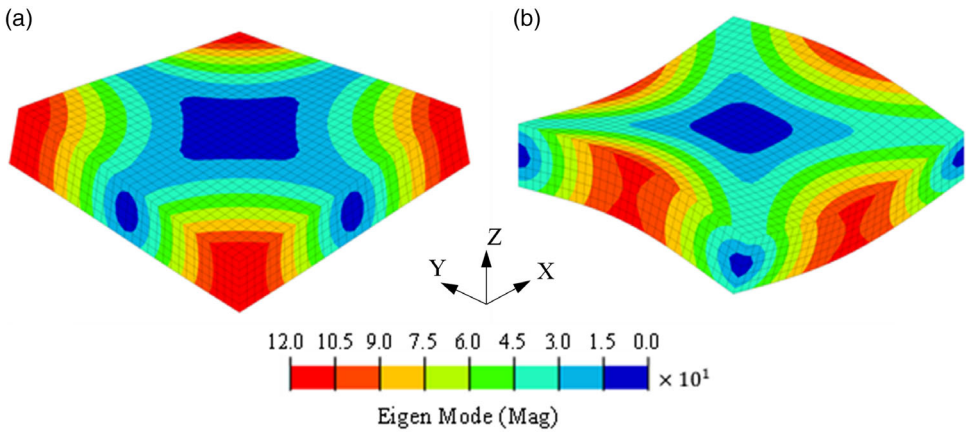

Figure 3. First two mode shapes and natural frequencies: a) 10 946 Hz and b) 16 241 Hz of the solid structure.

© 2023 The Authors. Advanced Engineering Materials published by Wiley-VCH GmbH

15272648, 2023, 11, Downloaded from https://onlinelibrary.wiley.com/doi/10.1002/adem.202201811 by Ozyegin University, Wiley Online Library on [06/09/2023]. See the Terms and Conditions (https://onlinelibrary.wiley.com/terms-and-conditions) on Wiley Online Library for rules of use; OA articles are governed by the applicable Creative Commons License

Once the geometrical and mechanical properties are linked, the topology optimization is performed using solid isotropic material penalization (SIMP). Prior to the lattice characterization, the number of lattice configurations and its mesh size for the FEM models are determined from the configuration and mesh convergence analysis, respectively. Thanks to previous studies, the number of configurations is defined as at least $5 \times 5 \times 5$-unit cells and more for configuration-independent lattice characterization.[53,54] As a result, $5 \times 5 \times 5$-unit cells in the x, y, and z-directions are adequate for properly calculating the elastic modulus of the lattices. **Figure 4** illustrates the solid mesh-based lattice models of $5 \times 5 \times 5$ lattice configuration for D-, G-, and I-WP-type lattices. As the $12 \times 12 \times 12$ mm lattice unit cells are used in the FEM models, the overall size of the structures is $60 \times 60 \times 60$ mm. Determination of the average mesh size for each lattice type is also an important factor for good correlation with modal testing. Therefore, a mesh convergence analysis was performed to determine the ultimate mesh size for each lattice type. In the thickness direction, the number of elements was raised from 2 to 12 with an increment of 1. The results have revealed that employing eight elements in the thickness direction for D- and G-type lattices, and four elements for I-WP-type lattices resulted in a relative accuracy of less than 1%. Therefore, the mesh size corresponding to eight elements in the thickness direction is used in FEM for subsequent analyses.

The homogenization of the lattice structures can be studied once the configuration and mesh size-independent structures for each lattice have been determined. The noncontinuum and periodic lattice structures are characterized using Steven's numerical technique.[55,56] In orthogonal systems, this technique exploits symmetry to decrease the number of unknowns from 81 to 21.[57] A unit strain is applied to the lattices in one direction while the rest are kept zero, as shown in Equation (6)[58]

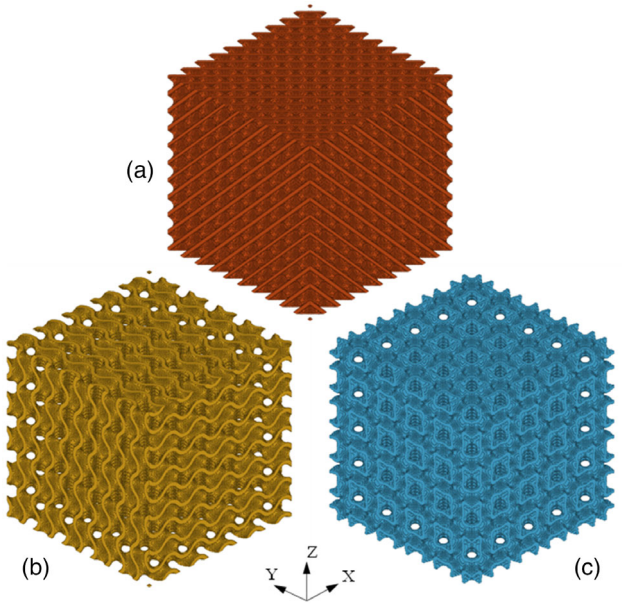

Figure 4. FEM model of $5 \times 5 \times 5$-unit cells lattice configuration of a) D-, b) G-, and c) I-WP-type lattice structures with $\rho^* = 0.3$.

$$\text{Input}: \begin{Bmatrix} \varepsilon_{11} \\ \varepsilon_{22} \\ \varepsilon_{33} \\ \varepsilon_{23} \\ \varepsilon_{31} \\ \varepsilon_{12} \end{Bmatrix} = \begin{Bmatrix} 1 \\ 0 \\ 0 \\ 0 \\ 0 \\ 0 \end{Bmatrix} \quad \text{Output}: \begin{Bmatrix} \sigma_{11} \\ \sigma_{22} \\ \sigma_{33} \\ \sigma_{23} \\ \sigma_{31} \\ \sigma_{12} \end{Bmatrix} = \begin{Bmatrix} C_{11} \\ C_{22} \\ C_{33} \\ C_{23} \\ C_{31} \\ C_{12} \end{Bmatrix} \tag{6}$$

Two distinct boundary conditions (BCs) are used to get the stiffness constants. In the first BC, as shown in Equation (7), a normal strain is applied to $5 \times 5 \times 5$ lattice configuration

$$\begin{aligned} &\Delta l_x\Big|_{x=l_x} = 0.001 l_x \\ &\Delta l_x\Big|_{x=0} = \Delta l_y\Big|_{y=l_y} = \Delta l_y\Big|_{y=0} = \Delta l_y\Big|_{y=l_y} = \Delta l_z\Big|_{z=0} = 0 \end{aligned} \tag{7}$$

where $l_x = 60$ mm for the unit cell size of $5 \times 5 \times 5$ mm in x, y, and z directions. Therefore, 0.06 mm displacement is applied to nodes at x plane at $x = l_x$ in the normal direction, while the displacement is set to be zero for all other planes. Then, half of the normal strain is applied on two planes for the shear strain, as shown in Equation (8)

$$\begin{aligned} &\Delta l_x\Big|_{z=l_x} = 0.0005 l_z, \Delta l_z\Big|_{x=l_z} = 0.0005 l_x \\ &\Delta l_z\Big|_{x=0} = \Delta l_y\Big|_{y=l_y} = \Delta l_y\Big|_{y=0} = \Delta l_z\Big|_{z=l_z} = \Delta l_x\Big|_{z=0} = 0 \end{aligned} \tag{8}$$

The effective stiffness matrix is computed from Equation (9) once the displacement and reaction forces on the boundaries have been determined as shown below

$$C_{ij}^C = \begin{bmatrix} C_{11} & C_{12} & C_{12} & 0 & 0 & 0 \\ C_{12} & C_{11} & C_{12} & 0 & 0 & 0 \\ C_{12} & C_{12} & C_{11} & 0 & 0 & 0 \\ 0 & 0 & 0 & C_{44} & 0 & 0 \\ 0 & 0 & 0 & 0 & C_{44} & 0 \\ 0 & 0 & 0 & 0 & 0 & C_{44} \end{bmatrix} \tag{9}$$

Finally, the elastic modulus can be calculated from Equation (10)

$$E_{\text{latt.}} = \frac{C_{11}^2 + C_{11}C_{12} - 2C_{12}^2}{C_{11} + C_{12}} \tag{10}$$

The relative density and corresponding relative elastic modulus, E^*, of different lattices are then generalized using the Gibson–Ashby model. The results are plotted in **Figure 5**. The relationship between the relative elastic modulus and the relative density appears similar for lattices for lower ρ^* values. More specifically, for lower relative densities, the D-type lattice has a higher elastic modulus than the other lattices. In contrast, the I-WP-type lattice performs better at higher relative density levels.

The constant parameters of the Gibson–Ashby model, C and p are summarized in **Table 2**. The exponents in the Gibson–Ashby model for D, G, and I-WP types are 1.275, 1.410, and 1.598, respectively. As previously stated, the value of p displays the lattice's deformation properties in terms of bending and stretching.

© 2023 The Authors. Advanced Engineering Materials published by Wiley-VCH GmbH

15272648, 2023, 11, Downloaded from https://onlinelibrary.wiley.com/doi/10.1002/adem.202201811 by Ozyegin University, Wiley Online Library on [06/09/2023]. See the Terms and Conditions (https://onlinelibrary.wiley.com/terms-and-conditions) on Wiley Online Library for rules of use; OA articles are governed by the applicable Creative Commons License

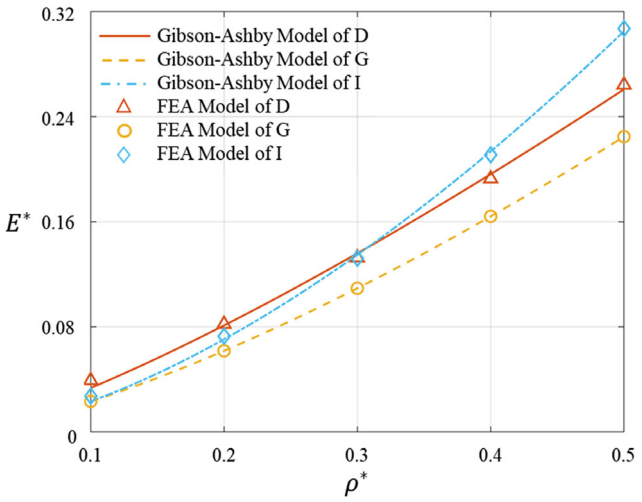

Figure 5. The FEM results and Gibson–Ashby models for D-, G-, and I-WP-type lattice structures.

Table 2. Gibson–Ashby parameters for D-, G-, and I-WP-type lattices.

Lattice type	Coefficient, C	Exponent, p
D	0.6310	1.275
G	0.5972	1.410
I-WP	0.9232	1.598

3.1.2. Modified SIMP

The SIMP algorithm, which relates the relative density of a finite element to elastic modulus using Equation (11), is one of the most used mathematical forms of the TO approaches

$$E_e = E_s(\rho_e)^p \tag{11}$$

where E_e and ρ_e are the elastic modulus and the relative density of the eth finite element, respectively, and $p(p \geq 1)$ is the penalization factor. Simsek et al.[24] proposed a modified SIMP method based on the Gibson–Ashby model to represent lattice properties and consider the intermediate element densities in the HMTO algorithm as shown in Equation (12)

$$E_e/E_s = C_1^*(\rho_e)^{p^*} \tag{12}$$

where C_1^* and p^* are the constants of the Gibson–Ashby. Different penalization factors on the relative elastic modulus are shown for D-, G-, and I-WP-type lattices in **Figure 6**.

3.1.3. Application of HMTO to the Case Study

The FEM models of the D-, G-, and I-WP-type lattices used in HMTO are shown in **Figure 7**a–c. The design domain consists of 5400 solid elements with size $2 \times 2 \times 2$ mm, while the lower and upper plates are composed of 450 quad shell elements with an average mesh size of 2 mm and their thickness is 0.8 mm.

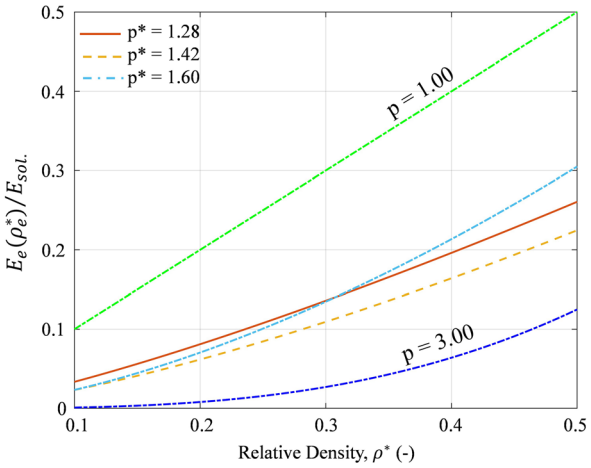

Figure 6. Comparison of SIMP models for varying penalty factors.

The utilization of a uniform mesh distribution in both the core region and plates enables a seamless node-to-node connection, facilitating the connection between the plates and core region. The constitutive elastic modulus (236 GPa) is scaled by 0.6310, 0.5972, and 0.9232 for D-, G-, and I-WP-type lattices, respectively. In the HMTO model, the minimum and maximum density values of the design domain, ρ_{min} and ρ_{max}, are set to 0.1 and 0.5, respectively. The limit for volume fraction is set to 0.3. The lower and upper limits for the first and second frequency bandgap are 8800 and 13 200 Hz, respectively. While exciting the structure with a unit load, the HMTO's goal is to minimize the sum of the acceleration spectrum obtained from nine response points. Equation (13) shows the formulation of the optimization problem based on HMTO models

$$\begin{aligned} &\min \textstyle\sum_{i=6000}^{15000} (\mathrm{RSS}(\omega))_i \\ &\text{s.t} \textstyle\sum_{e=1}^{n} \rho_e V_e < \alpha V_0 \\ &0 \leq \rho_{min} \leq \rho_e \leq \rho_{max} \leq 1 \\ &f_l \leq 8800\,\text{Hz} \\ &f_u \geq 13200\,\text{Hz} \end{aligned} \tag{13}$$

where f_l and f_u specify the lower and upper limits of the frequency bandgap, respectively. This enforces that the structure will not have any natural frequency between f_l and f_u.

Figure 8 shows the optimum material (or density) distribution for the D-, G-, and I-WP-type lattice structures. It is observed that the relative densities are higher toward the edges. This is primarily due to the first mode shape of the structure (see Figure 3a). The results also reveal that material models for the D and I-WP lattice structures respond differently than the material models for G-type lattice structures. The constant parameters of the material model of the G-type lattice allow for a smoother transition in the density distribution. The volume fraction of 0.3 constraint has been met for three types of the lattices. Also, the design goal relating to the bandgap is fulfilled for all lattice types. For D-, G-, and I-WP-type lattices, the first modes are found at 8022, 7993, and 7624 Hz, respectively. Also, the second modes of optimal structures are 16 310, 16 023, and 16 169 Hz, respectively.

© 2023 The Authors. Advanced Engineering Materials published by Wiley-VCH GmbH

15272648, 2023, 11, Downloaded from https://onlinelibrary.wiley.com/doi/10.1002/adem.202201811 by Ozyegin University, Wiley Online Library on [06/09/2023]. See the Terms and Conditions (https://onlinelibrary.wiley.com/terms-and-conditions) on Wiley Online Library for rules of use; OA articles are governed by the applicable Creative Commons License

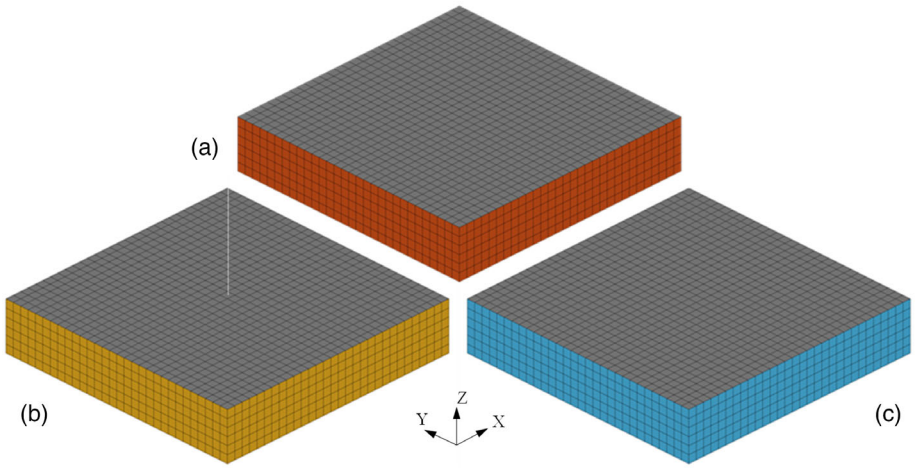

Figure 7. FEM models used in the HMTO for the a) D-, b) G-, and c) I-WP-type lattices.

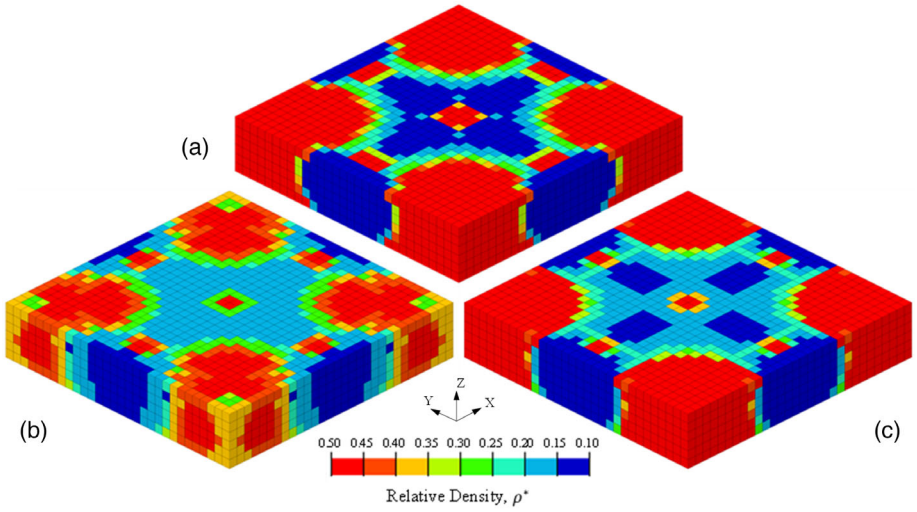

Figure 8. Optimal material distribution obtained from the application of HMTO method for a) D-, b) G-, and c) I-WP-type lattice structures.

3.2. FOGLG

The HMTO is a useful method for various lattice structures to obtain an optimal material distribution of the design domain. As part of the preoptimization process, this method may be utilized on any lattice structure that can be homogenized. On the other hand, the design flexibility of shell element-based lattice modeling is also attractive in optimization approaches. As a result, the FOGLG method for modal characterization of sandwiched structures will be detailed next, which involves shell-based lattice modeling.

3.2.1. Modeling of Lattices with Shell Elements

The FOGLG, which is based on shell modeled lattices structures, is the second optimization technique investigated in this study. **Figure 9** shows the shell element-based models for a single unit cell of 12 mm size for D-, G-, and I-WP-type lattices. The lattice structure is modeled with 2D four-noded quadrilateral mesh elements in this approach.

In the 2D shell models of the lattice structures, the ρ^* is directly dependent on the shell thickness, T. There is a unique relation between T and ρ^* for each lattice. These unique relations between T and ρ^* are given in Equation (14a), (14b), and (14c) for D, G, and I-WP lattice structures, respectively.

$$\rho^*{}_{\mathrm{D}} = 0.32005 \times T_{\mathrm{D}} \tag{14a}$$

$$\rho^*{}_{\mathrm{G}} = 0.25781 \times T_{\mathrm{G}} \tag{14b}$$

$$\rho^*{}_{\mathrm{I-WP}} = 0.29623 \times T_{\mathrm{I-WP}} \tag{14c}$$

The authors previously demonstrated that the accuracy of shell models is relatively high for lower relative densities.[25,34] A similar study is performed here to quantify the accuracy of different models for the optimization problem. First, the mechanical properties of lattices are compared using the shell (see Figure 9) and

© 2023 The Authors. Advanced Engineering Materials published by Wiley-VCH GmbH

15272648, 2023, 11, Downloaded from https://onlinelibrary.wiley.com/doi/10.1002/adem.202201811 by Ozyegin University, Wiley Online Library on [06/09/2023]. See the Terms and Conditions (https://onlinelibrary.wiley.com/terms-and-conditions) on Wiley Online Library for rules of use; OA articles are governed by the applicable Creative Commons License

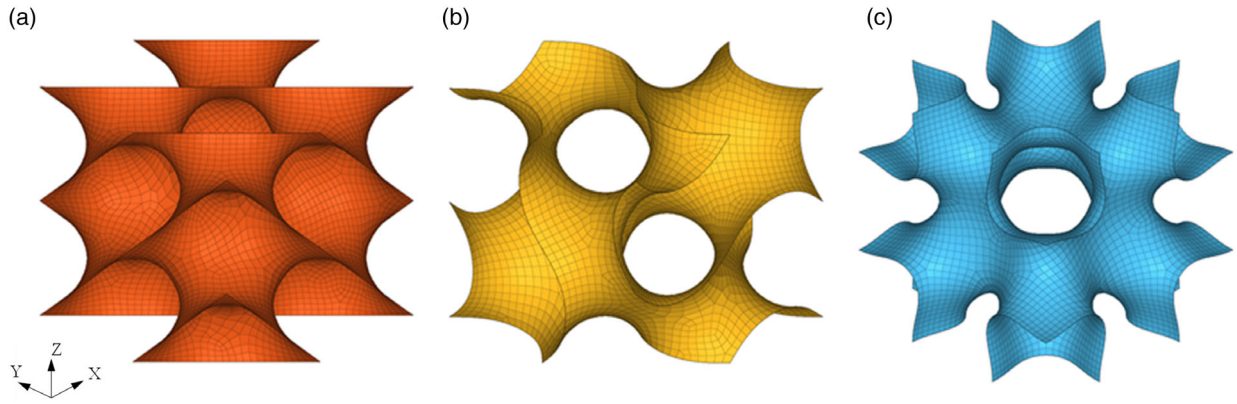

Figure 9. Shell-based models of single unit cell a) D, b) G, and c) I-WP lattice types.

solid (see Figure 4) element-based models. For D-, G-, and I-WP-type lattices, the mesh size is determined from a similar mesh convergence analysis. The volume fraction is varied from 0.1 to 0.5 with an increment of 0.1. The average mesh size of each model is calculated by dividing its unit cell size of 12 mm by a constant i ranging from 10 and 40 in increments of 5. More specifically, the maximum and minimum mesh sizes used in FEM of the lattice structures are calculated as 2.4 and 0.3 mm, respectively. Similarly, the ultimate mesh size for D- and I-WP-type lattice structures is determined as 0.35 and 0.4 mm for G-type lattices. Then boundary conditions are applied as outlined in Section 3.1.1 to find out stiffness values of the lattice structures. The calculated values of the C_{11}, C_{12}, and C_{44} for shell and solid models are compared in **Figure 10**a–c.

The effective stiffness values of the shell element and solid element-based lattice modeling show that the degree of accuracy of the solid and shell meshing depends on the lattice type and relative density. **Table 3** shows the relative error between the two modeling approaches for various lattice types. The results indicate that the relative error between the solid and shell element-based modeling for D-type lattice varies from 0.3% and 6.7%. The relative error value is between 0.9% and 5.3% for G-type lattices. Even though the maximum relative error for I-WP-type lattice structure is 16.4% at 0.5 volume fraction, it is only 7.1% for 0.3 volume fraction.

It can be observed that at higher relative density, the transverse shear effects and curved shape of the structures cause a discrepancy between the solid and shell element-based lattice modeling. Yet, the results suggest that the accuracy of the shell models is comparable to the accuracy of solid models at lower volume ratios. Therefore, the shell modeling is used as an alternative to solid modeling at lower volume ratios.

3.2.2. Application of FOGLG to the Case Study

The constraint and objective of the FOGLG optimization are the same as described in Section 3.1.3. However, because the T value is one of the design factors for the shell modeled lattices, the optimization design variables for the FOGLG models are updated as the thicknesses of shell models. The formulation of the FOGLG is given in Equation (15)

$$\begin{aligned} &\min \textstyle\sum_{i=6000}^{15000} (\mathrm{RSS}(\omega))_i \\ &\text{s.t } \textstyle\sum_{e=1}^{m} T_e A_e \le \alpha V_0 \\ &T_{\mathrm{lb}} \le T \le T_{\mathrm{ub}} \\ &f_1 \le 8800\ \mathrm{Hz} \\ &f_u \ge 13200\ \mathrm{Hz} \end{aligned} \tag{15}$$

where T_{lb} and T_{ub} are lower and upper limits on the shell thickness, respectively. A_e is the area of the eth shell element, and m represents the number of shell elements in FEM. The average mesh size of FE model of the D-type lattice structure is 0.3 mm. In the design domain, there are 150 000 quad and tria elements. The average mesh size for the I-WP-type lattice is 0.31 mm, which corresponds to 130 000 finite elements. Due to its simpler geometry compared to the D- and I-WP-type lattices, the G-type lattice has a mesh size of 0.37 mm. In the design domain of the FEM model of the G-type lattice, there are 83 000 quad and tria elements. The plates are modeled with a total number of 27 000 2D quad elements. The interaction between the core region and plates is represented by a node-to-node connection using a uniform mesh size with a lattice type structure. The FEM models used in FOGLG for the D-, G-, and I-WP-type lattices are shown in **Figure 11**a–c, respectively.

Figure 12 illustrates optimum relative density distribution obtained from the FOGLG for D-, G-, and I-WP-type lattice structures. The results demonstrate that the material distribution is similar to that obtained by the application of HMTO. The relative densities are higher in the parts of the structure where there is a considerable deformation. The results show that D- and I-WP-type lattices have sharper transitions, but G-type lattices have smoother transitions.

The designs obtained by using the FOGLG algorithm meet the volume fraction and bandgap criteria. For the D-, G-, and I-WP-type lattices, the initial natural frequency is 7302, 8328, and 7258 Hz, respectively. The second natural frequencies of the optimized designs are 16 258, 15 976, and 16 102 Hz for the D-, G-, and I-WP-type lattices, respectively.

In **Figure 13**, the objective functions for HMTO and FOGLG are compared. For the D-, G-, and I-WP-type lattices, the starting point difference is 5.1%, 4.3%, and 5.8%, respectively. This

© 2023 The Authors. Advanced Engineering Materials published by Wiley-VCH GmbH

15272648, 2023, 11, Downloaded from https://onlinelibrary.wiley.com/doi/10.1002/adem.202201811 by Ozyegin University, Wiley Online Library on [06/09/2023]. See the Terms and Conditions (https://onlinelibrary.wiley.com/terms-and-conditions) on Wiley Online Library for rules of use; OA articles are governed by the applicable Creative Commons License

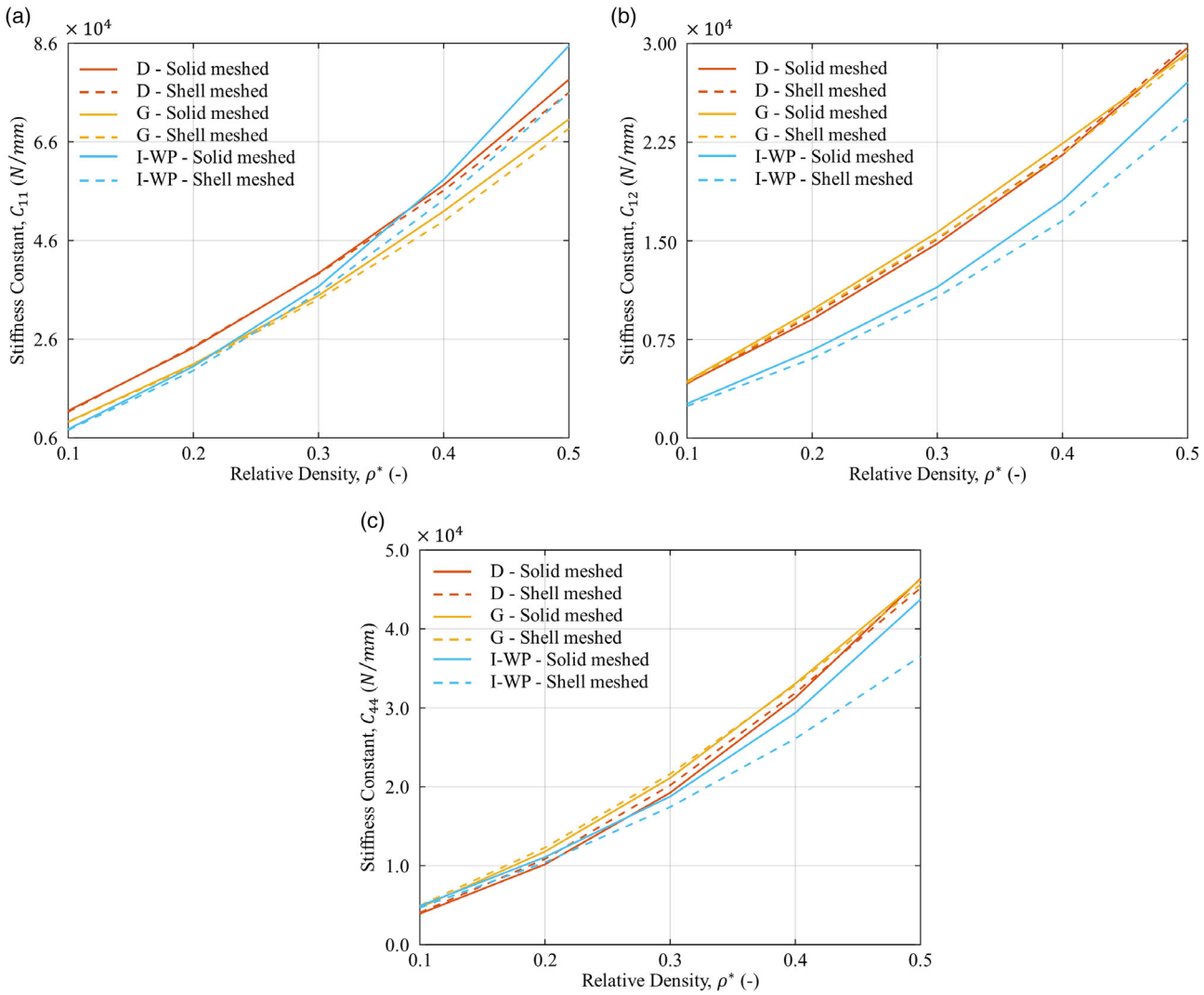

Figure 10. Solid versus shell modeling comparison in terms of effective stiffness, C_{11}, C_{12},and C_{44} of a) D-, b) G-, and c) I-WP-type lattices.

Table 3. Relative error of effective stiffness constants C_{11}, C_{12}, and C_{44} between shell and solid based modeled D-, G-, and I-WP-type lattice structures.

VF	% Relative error (D type)			% Relative error (G type)			% Relative error (I-WP type)		
	C_{11}	C_{12}	C_{44}	C_{11}	C_{12}	C_{44}	C_{11}	C_{12}	C_{44}
0.1	2.0	1.0	3.5	0.9	2.7	5.3	2.3	6.9	4.3
0.2	1.0	3.5	6.7	1.2	2.5	4.3	4.1	9.5	6.0
0.3	0.3	2.2	5.0	2.2	2.8	2.4	3.3	6.5	7.1
0.4	1.9	1.1	1.9	3.9	3.7	0.6	7.1	8.7	11.1
0.5	3.3	0.9	2.6	2.7	0.6	1.3	11.2	10.2	16.4

difference is attributed to the discrepancy in element formulation between the solid and shell-based modeling techniques. The value of the objective function for the FOGLG model is higher than that of the HMTO model in the first iteration. This means that the FOGLG model is less stiff than the HMTO model. The value of the objective function in the final iteration of the FOGLG for the D-, G-, and I-WP-type lattices is 10.4%, 1.9%, and 8.4% lower than the HMTO, respectively. The volume fraction requirement of 0.3 is met using all optimization methodologies. Both algorithms also meet the frequency bandgap requirement of no resonance frequencies between 8800 and 13 200 Hz.

© 2023 The Authors. Advanced Engineering Materials published by Wiley-VCH GmbH

15272648, 2023, 11, Downloaded from https://onlinelibrary.wiley.com/doi/10.1002/adem.202201811 by Ozyegin University, Wiley Online Library on [06/09/2023]. See the Terms and Conditions (https://onlinelibrary.wiley.com/terms-and-conditions) on Wiley Online Library for rules of use; OA articles are governed by the applicable Creative Commons License

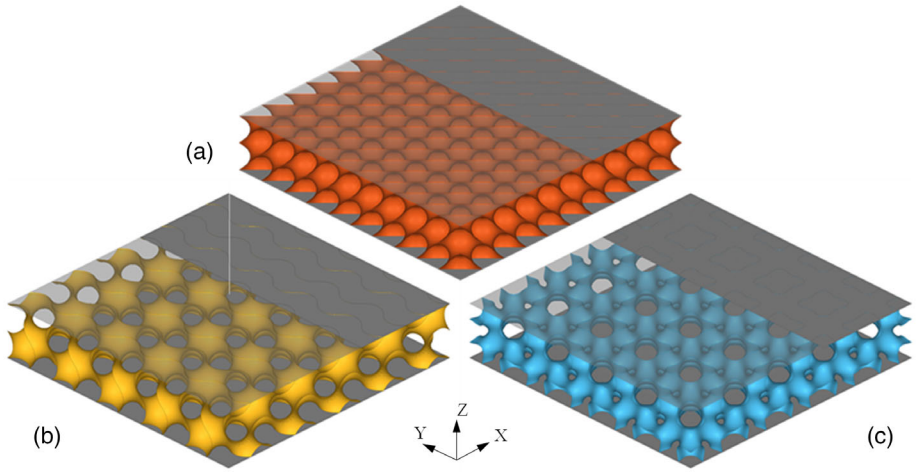

Figure 11. The FEM models used in FOGLG of the a) D-, b) G-, and c) I-WP-type lattices (left part of the upper plate is intentionally made transparent for better visualization of the design domain filled with lattice structures).

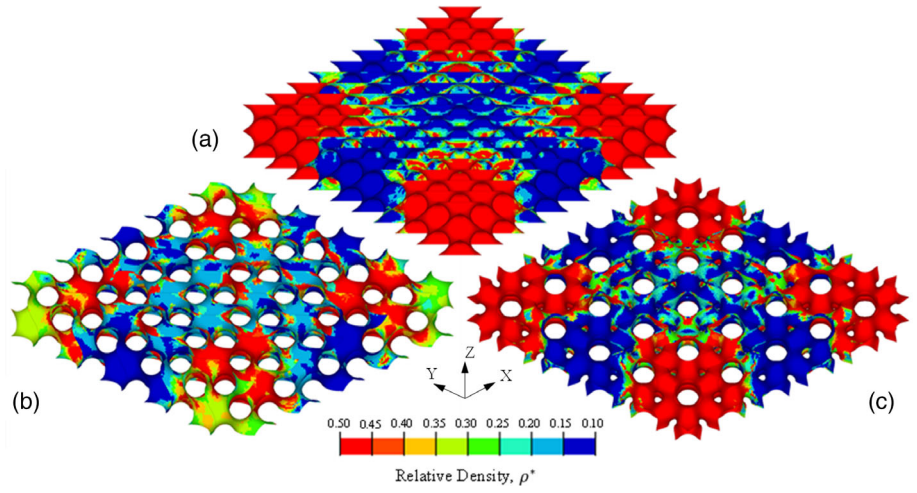

Figure 12. Optimal material distribution designs obtained from the FOGLG method for a) D-, b) G-, and c) I-WP-type lattice structures.

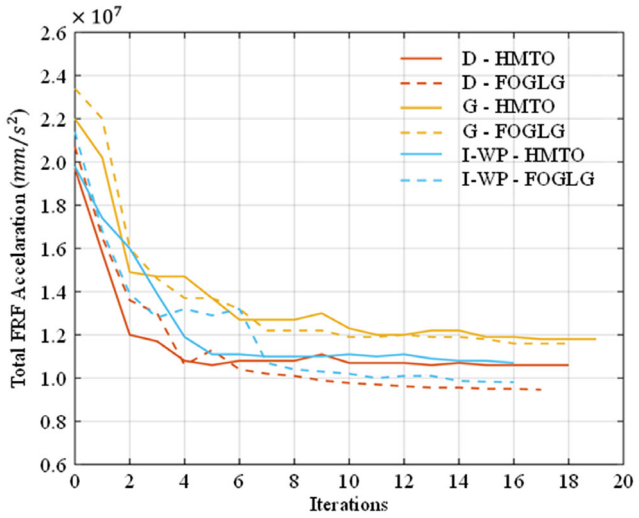

Figure 13. Optimization results of HMTO and FOGLG methods.

3.3. Reconstruction of HMTO Models via Relative Density Method

The optimum models obtained by the application of HMTO are reconstructed using the relative density method (RDM). This reconstruction algorithm is chosen considering its applicability to FEM models with solid elements. The flowchart of the overall RDM is given in **Figure 14**. For an overview of RDM algorithm, the reader is referred to the literature.[35]

The RDM algorithm consists of four steps. First, the ideal relative densities are acquired from HMTO, and the coordinates of each element's centroid are retrieved. The corner nodes acquired in step 1 are then assigned with their density values. Equation (16) is then used to conduct arithmetic averaging of the element densities[35]

$$\rho_{xyz} = \frac{\sum X^*_{xyz}}{N_{\text{node}}} \tag{16}$$

© 2023 The Authors. Advanced Engineering Materials published by Wiley-VCH GmbH

15272648, 2023, 11, Downloaded from https://onlinelibrary.wiley.com/doi/10.1002/adem.202201811 by Ozyegin University, Wiley Online Library on [06/09/2023]. See the Terms and Conditions (https://onlinelibrary.wiley.com/terms-and-conditions) on Wiley Online Library for rules of use; OA articles are governed by the applicable Creative Commons License

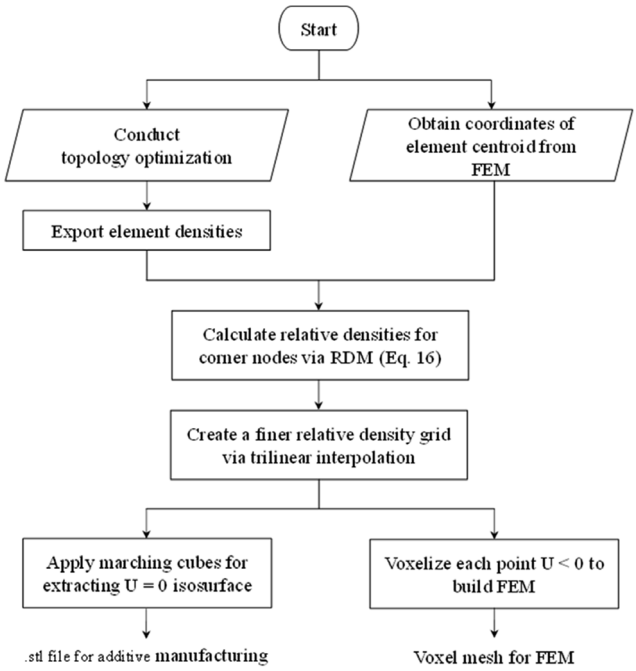

Figure 14. Flowchart for the reconstruction of optimized design utilizing RDM.

where ρ_{xyz} is the arithmetic average of the relative densities, and N_{node} stands for the node number. Intermediate densities are linearly interpolated in the design domain as given in Equation (17)

$$\rho_{xi} = \rho_{xb} - (\rho_{xb} - \rho_{xa}) \frac{x_b - x_i}{x_b - x_a} \tag{17}$$

where a and b are two locations on the x-axis. For the design domain, a linear averaging proportional to the distance between specified points is used. As a result, in the third step, linear averaging of numerous points enables the creation of a finer mesh grid with an averaged relative density matrix. The final step of the RDM is to export the lattices according to the relative densities obtained from the HMTO method. The first export option is to use voxelization, which uses eight-node hexahedral mesh elements, for the FEM at the lattice at isosurface $U < 0$ for the FEM, as shown in **Figure 15**b, **16**b, and **17**b. Applying the marching cubes algorithm and obtaining the model at isosurface $U = 0$ is the second export option of the extraction of the reconstructed geometries.[59] Once the marching cubes for each lattice type have been collected, they are transformed into .stl format, which is a 2D triangular mesh model required for 3D printing (see Figure 15b, 16b, and 17b).

Based on the implicit lattice formulas presented in Equation (2a), (2b), and (2c), the RDM method is applied to D, G, and I-WP types of lattices. The RDM algorithm is used to construct the D-type lattice initially. Figure 15b represents the voxel form of the lattice structure. By comparing the thickness of the reconstructed design to the optimum design from HMTO (see Figure 15a), the accuracy of the reconstructed design is confirmed. The comparison results show that the thickness gradient is the same for both designs. In addition, the relative error between the relative density of optimized and reconstructed design is less than 2% for D-type lattice structure. The .stl format of the D-type structure for 3D printing is shown in Figure 15c.

A similar reconstruction approach is then studied individually for G- and I-WP-type lattices. Figure 16 and 17 represent the optimization results, voxel mesh, and .stl form of the reconstructed geometries of the G- and I-WP-type lattices, respectively.

After preliminary tests on the thickness variation and relative density, the dynamic performance of the reconstructed designs is determined by calculating their FRF. **Figure 18** compares the FRF of the optimized design from HMTO with the reconstructed design for D-, G-, and I-WP-type lattices. For D, G, and I-WP types, the relative error for the first natural frequency is only 3.0%, 3.3%, and 2.9%, respectively. The comparison results show that the order of accuracy for the reconstruction is sufficient for the printing of the specimens for the experiment.

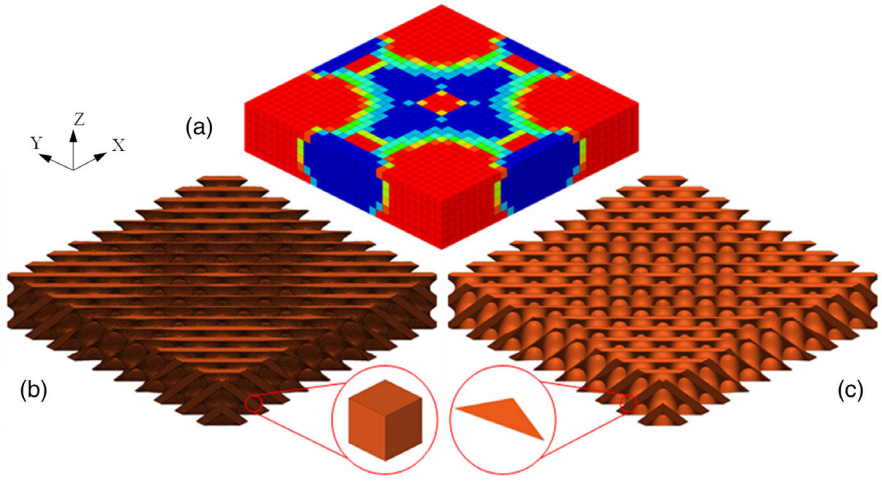

Figure 15. Reconstruction process of the HMTO method for the D-type lattice: a) optimization results, b) the voxelization of the reconstructed geometry, and c) reconstructed geometry in .stl format.

© 2023 The Authors. Advanced Engineering Materials published by Wiley-VCH GmbH

15272648, 2023, 11, Downloaded from https://onlinelibrary.wiley.com/doi/10.1002/adem.202201811 by Ozyegin University, Wiley Online Library on [06/09/2023]. See the Terms and Conditions (https://onlinelibrary.wiley.com/terms-and-conditions) on Wiley Online Library for rules of use; OA articles are governed by the applicable Creative Commons License

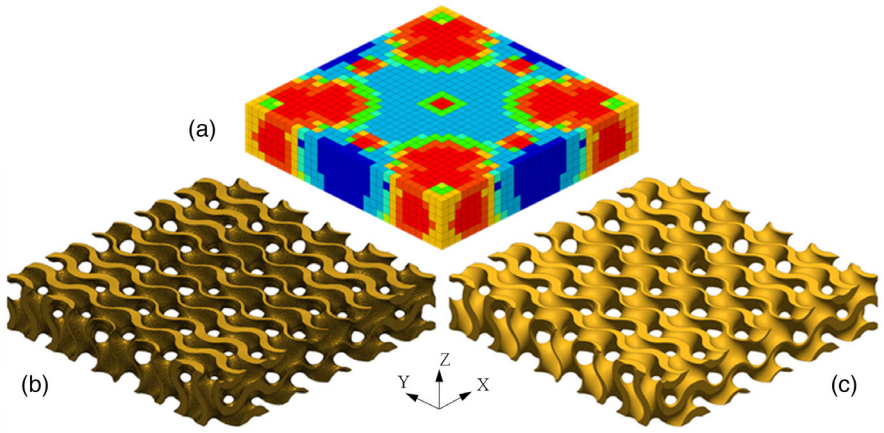

Figure 16. Reconstruction process of the HMTO method for the G-type lattice: a) optimization results, b) the voxelization of the reconstructed geometry, and c) reconstructed geometry in .stl format.

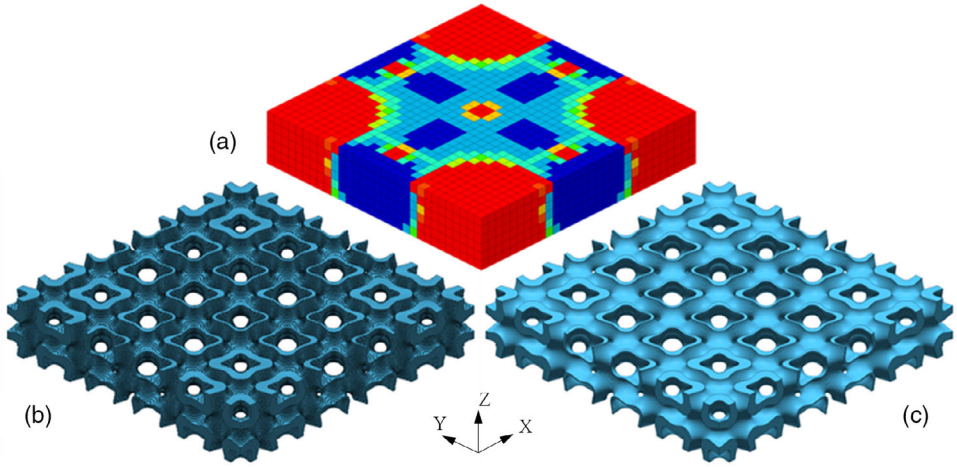

Figure 17. Reconstruction process of the HMTO method for the I-WP-type lattice: a) optimization results, b) the voxelization of the reconstructed geometry, and c) reconstructed geometry in .stl format.

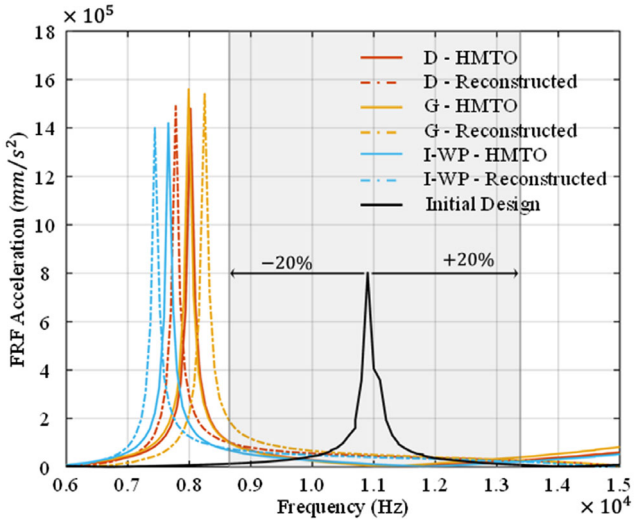

Figure 18. The FRF comparison: reconstructed design versus HMTO design.

3.4. Reconstruction of FOGLG Models via Enhanced RDM

The enhanced RDM (ERDM) reconstruction approach is adopted because the FOGLG employs shell models for the lattices. For G-, D-, and I-WP-type lattices, Equation (14a), (14b), and (14c) are used to convert the optimal thickness of the shell elements from FOGLG to the ρ^* values. Then, the values of ρ^* are assigned to the centroid of the corresponding shell element. However, because the centroids of the shell elements are randomly distributed across the design area, the reconstruction process requires a temporary uniform point cloud. Therefore, the uniform point cloud is created with respect to the cell size and average mesh size using Equation (18)

$$D = \frac{\text{unit cell size}}{10 \times (\text{average mesh size})} \tag{18}$$

where D defines distance between two point of the created uniform point cloud (see **Figure 19**). Therefore, defining a large value for D parameter will result in a coarse point cloud which

© 2023 The Authors. Advanced Engineering Materials published by Wiley-VCH GmbH

15272648, 2023, 11, Downloaded from https://onlinelibrary.wiley.com/doi/10.1002/adem.202201811 by Ozyegin University, Wiley Online Library on [06/09/2023]. See the Terms and Conditions (https://onlinelibrary.wiley.com/terms-and-conditions) on Wiley Online Library for rules of use; OA articles are governed by the applicable Creative Commons License

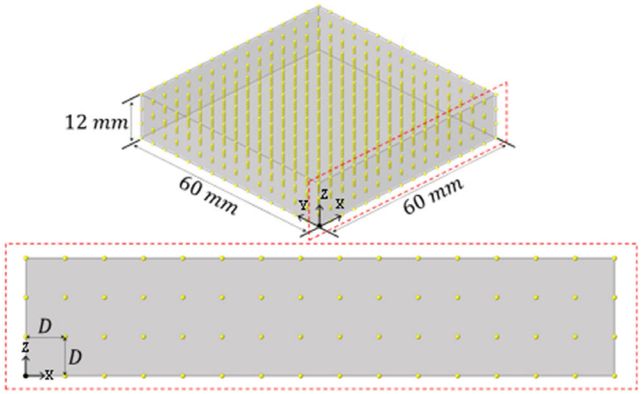

Figure 19. Schematic illustration of a uniform point cloud distribution in the 60 × 60 × 12 mm design domain.

decreases the reconstruction time. However, this may lead to miss some data at closer region. Therefore, defining an optimal D value is crucial for reconstruction process, so that it is related to unit cell size and average mesh size used in the FEM.

The average value of ρ^* values of the design domain is calculated using Equation (19).[60] The distance effect of the shell centroid is also taken into account using a weight function $w(r_{ij})$ given in Equation (20)

$$\rho_j = \frac{\sum_{i=1}^{m} \rho_i w(r_{ij})}{w(r_{ij})} \tag{19}$$

$$w(r_{ij}) = \exp(-r_{ij}^{s}) \tag{20}$$

where ρ_j is the calculated average ρ^* value of the temporary point of j; m is the total number of 2D mesh elements. The distance between the centroid of 2D element i and temporarily created point j is represented by r_{ij}. The parameter, s, is the smoothing factor that manipulates the distance effect. The parameters, D and s, affect the accuracy, quality, and computational efficiency of the reconstruction process. For example, increasing these parameters results in a smoother and more accurate reconstruction at the expense of increased computational time. Finally, the models are extracted into two forms: 1) marching cubes and 2) voxelized form. The marching cubes are then converted into .stl format for AM, while the voxelized form is used in the FEM. The flowchart of the ERDM is given in **Figure 20**. The reader is referred to the authors' previous study for the details of the ERDM algorithm.[34]

The optimal thickness distribution of the D-type lattice structure is shown in **Figure 21**a. The quality of the reconstructed model is assessed considering the thickness variation, and the volume fraction. These checks are carried out with the voxelized reconstructed model (see Figure 21b). The thickness variation of the optimized and voxelized designs is the same. Also, the average relative error of the relative density is less than 2% for all-lattice types. In order to manufacture the design using AM, the marching cubes format of the design is generated as depicted in Figure 21c.

The reconstruction process is repeated and validated for G- and I-WP-type lattices, respectively. The optimized design, voxel

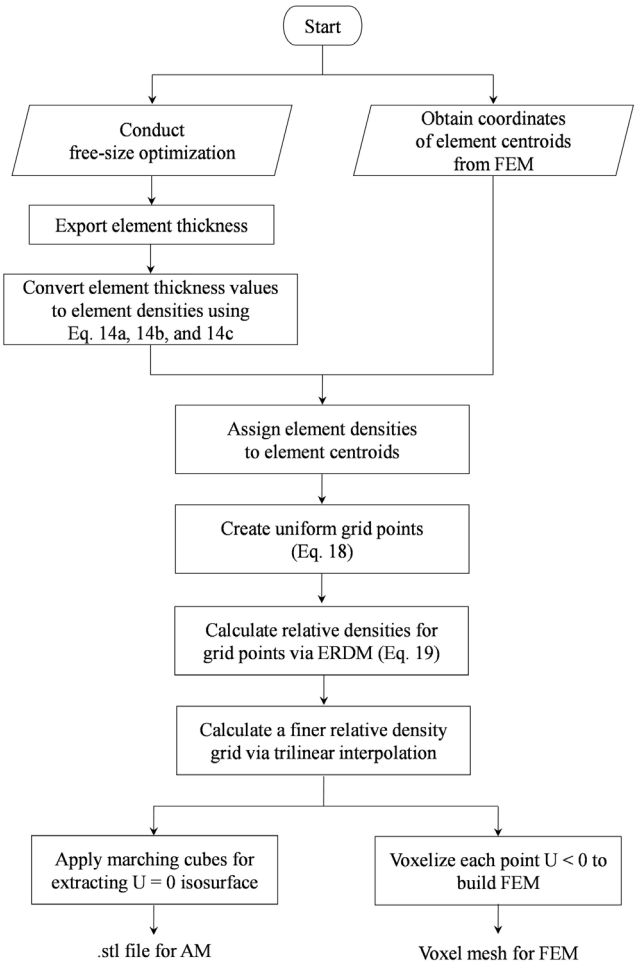

Figure 20. Flowchart for the reconstruction of optimized design utilizing ERDM.

mesh, and .stl form of the reconstructed geometries of G- and I-WP-type lattices are presented in **Figure 22**a–c and **23**a–c, respectively.

The FRFs of the reconstructed geometries are then compared to the optimal design using FOGLG method. **Figure 24** compares the FRF results of the reconstructed and optimized designs by the application of FOGLG.

The results demonstrate that the peak amplitudes are quite similar. For the G, D, and I-WP type, the relative error in the first natural frequency between the reconstructed and optimized models is 1.9%, 2.2%, and 1.8%, respectively. These results suggest that the ERDM reconstruction approach is effective.

4. Fabrication and Experimental Validation

The reconstructed geometries are manufactured with 3D printer using the DMLM process. A Concept Laser M2 DMLM printer (Concept Laser GmbH, GE Additive, Germany) is used for this process. At each layer, a 50 μm layer is degraded in an argon gas environment. **Figure 25**a–c shows the isometric and front view of the fabricated FGLs specimens designed by the HMTO method,

 © 2023 The Authors. Advanced Engineering Materials published by Wiley-VCH GmbH

15272648, 2023, 11, Downloaded from https://onlinelibrary.wiley.com/doi/10.1002/adem.202201811 by Ozyegin University, Wiley Online Library on [06/09/2023]. See the Terms and Conditions (https://onlinelibrary.wiley.com/terms-and-conditions) on Wiley Online Library for rules of use; OA articles are governed by the applicable Creative Commons License

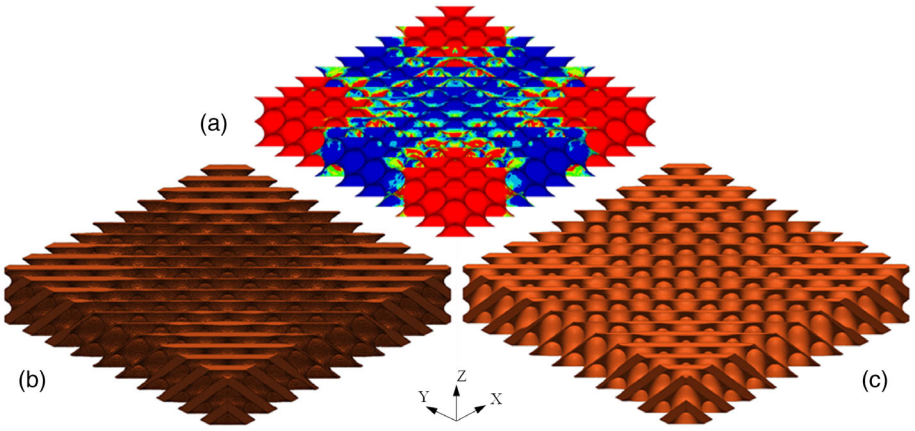

Figure 21. Reconstruction process of FOGLG method for the D-type lattice: a) the optimization results, b) the voxel meshed reconstructed geometry, and c) the .stl reconstructed geometry.

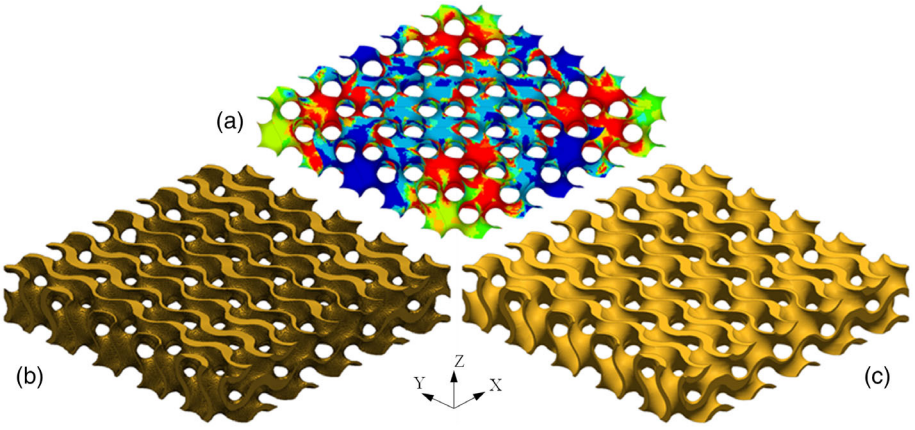

Figure 22. Reconstruction process of the FOGLG method for the G-type lattice: a) the optimization results, b) the voxelization of the reconstructed geometry, and c) reconstructed geometry in .stl format.

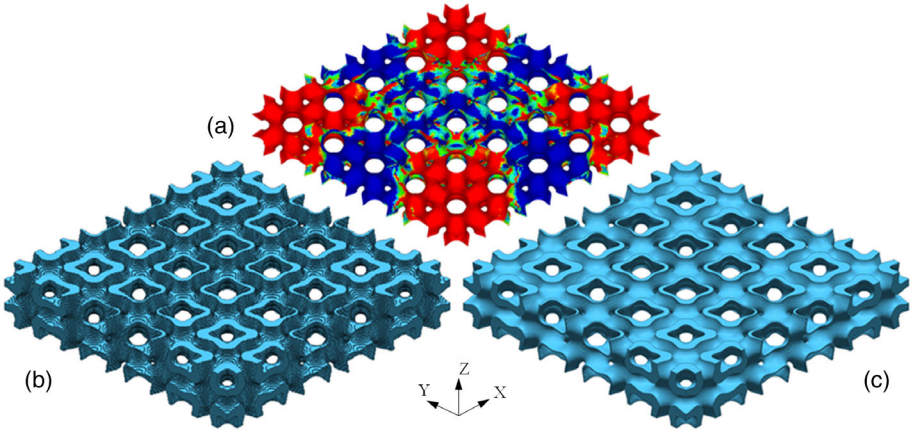

Figure 23. Reconstruction process of the FOGLG method for the I-WP-type lattice: a) the optimization results, b) the voxelization of the reconstructed geometry, and c) reconstructed geometry in .stl format.

and **Figure 26**a–c presents the fabricated specimens designed by the FOGLG method. To assess the accuracy of the fabricated geometries, the thickness variation is compared to FEM model used in the HMTO and FOGLG methods. From the fabricated specimens, it can be observed that the thickness grading from higher ($\rho^* = 0.5$) to lower ($\rho^* = 0.1$) relative density region

 © 2023 The Authors. Advanced Engineering Materials published by Wiley-VCH GmbH

15272648, 2023, 11, Downloaded from https://onlinelibrary.wiley.com/doi/10.1002/adem.202201811 by Ozyegin University, Wiley Online Library on [06/09/2023]. See the Terms and Conditions (https://onlinelibrary.wiley.com/terms-and-conditions) on Wiley Online Library for rules of use; OA articles are governed by the applicable Creative Commons License

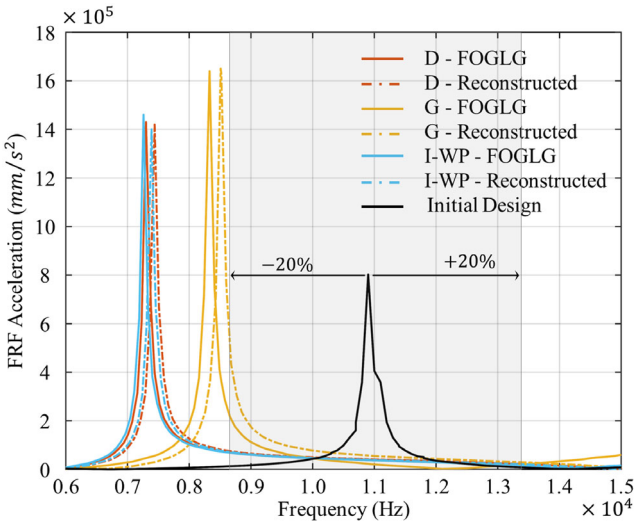

Figure 24. The FRF comparison: reconstructed design versus FOGLG design.

matches the thickness grading in the .stl models of the reconstructed geometries. Also, the nominal external dimensions of the fabricated specimens are in good agreement with the .stl, thanks to the high precision capability of AM.

In addition to the thickness variation, the average weight of the manufactured specimens was compared to the FEM model. The comparison results for samples designed using the HMTO and FOGLG methods are given in **Table 4**. The results demonstrate that the relative error between the mass of the fabricated specimens and FEM models is, on average, 5%, when all samples are considered. Therefore, this level of precision for mass and thickness grading is considered sufficient for modal testing to validate the FEM models.

Once the quality and accuracy of the fabricated specimens are confirmed, the modal characterization test is conducted to experimentally validate the proposed optimization approaches. The modal validation of the specimens is conducted by exciting them with a 7BB-41-2L0 piezo-buzzer with a negligible mass of 1.5 g.[61] The input voltage and frequency of the piezo are controlled by a waveform generator. Initially, a frequency range of 6–15 kHz with an increment of 100 Hz is determined. Once the system resonance is observed, the frequency increment is decreased to 1 Hz to capture the natural frequency with high accuracy. The displacements are measured by a PSV-400 Polytec laser vibrometer.[62] Reflectors are attached to the samples to reflect the laser from the laser vibrometer. The piezo buzzer is attached on the bottom face of the specimens at the point of interest, and the reflector is attached to top face for reflecting the laser to measure the displacement. To simulate free-to-free boundary condition used in FEM, the specimens are hung by thin wires. The experiment is repeated 3 times for each sample, and the average of the results is used in the comparison between the test and FEM. The experimental setup is shown in **Figure 27**.

The numerical and experimental test results of the six FGLs specimens designed by HMTO and FOGLG are presented in **Table 5** and **6**. The modal test is conducted in the frequency range of 6000 and 15 000 Hz for modal characterization of the printed FGLs. The natural frequencies of the test specimens are determined by reading the frequencies of the peak displacements from the test. From the comparison results, it is observed that there is a good agreement between the numerical and experimental results of the samples reconstructed by the RDM. More specifically, the relative error for the resonance frequency of the HMTO designed and fabricated D-, G-, and I-WP-type FGLs is 2.8%, 1.5%, and 0.7%, respectively. Similarly, the test specimens reconstructed by the ERDM approach have a better agreement in first resonance frequency. The relative error values are only 1.8%,

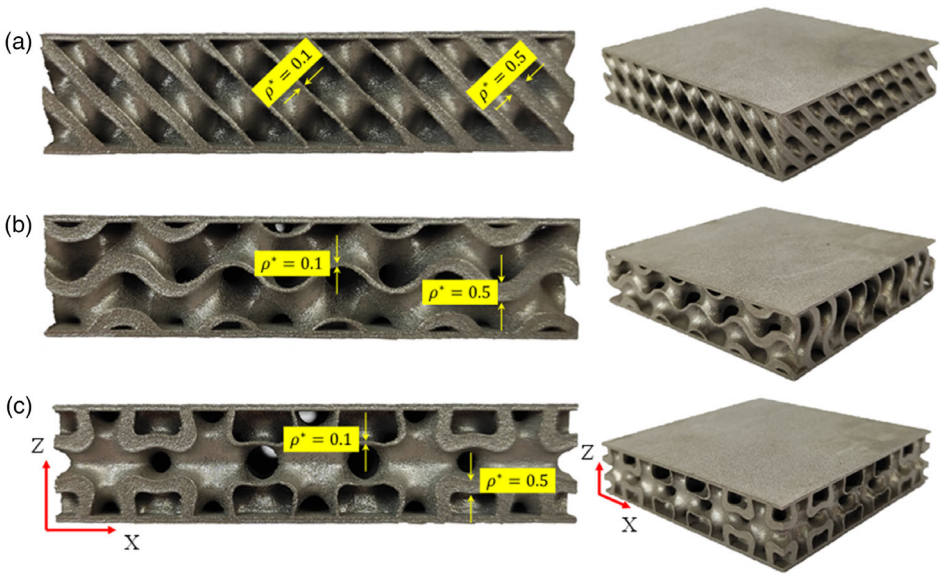

Figure 25. Additively fabricated specimens designed by the application of HMTO method: a) D-, b) G-, and c) I-WP-type structures.

© 2023 The Authors. Advanced Engineering Materials published by Wiley-VCH GmbH

15272648, 2023, 11, Downloaded from https://onlinelibrary.wiley.com/doi/10.1002/adem.202201811 by Ozyegin University, Wiley Online Library on [06/09/2023]. See the Terms and Conditions (https://onlinelibrary.wiley.com/terms-and-conditions) on Wiley Online Library for rules of use; OA articles are governed by the applicable Creative Commons License

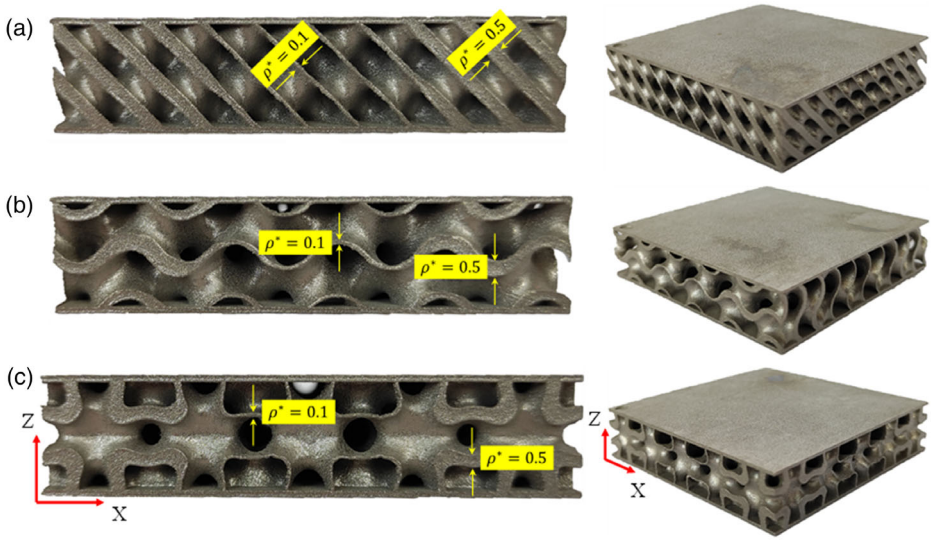

Figure 26. Additively fabricated specimens designed by the application of FOGLG method: a) D-, b) G-, and c) I-WP-type structures.

Table 4. Mass comparison of the FEM and fabricated FGLs lattices.

Lattice type	HMTO specimens			FOGLG specimens		
	FEA [g]	Fabricated [g]	Relative error [%]	FEA [g]	Fabricated [g]	Relative error [%]
D	155.5	148.6	4.5	156.4	148.7	4.9
G	155.0	147.5	4.8	155.1	147.9	4.7
I-WP	157.1	148.1	5.7	157.5	148.7	5.6

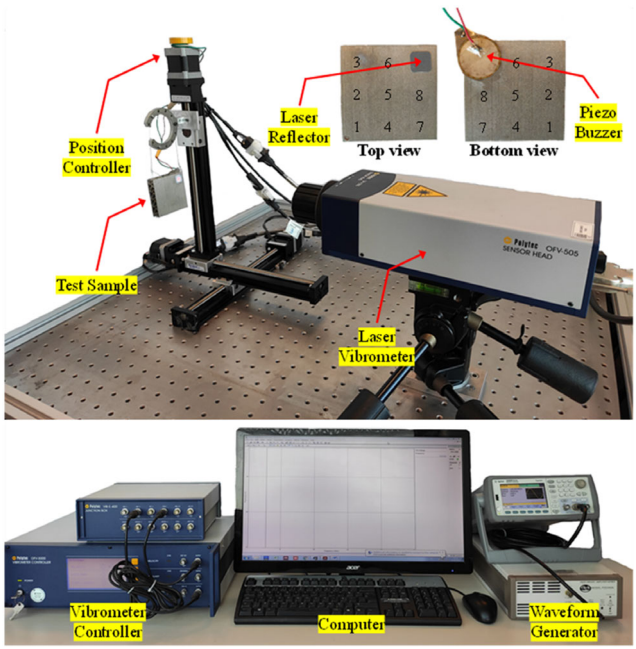

Figure 27. Experimental setup.

Table 5. Comparison of first resonance frequency between the FEM and experimental test results of the HMTO designed geometries.

Lattice type	FEM [Hz]	Experiment [Hz]	Relative error [%]
D	7780	7558	2.8
G	8242	8116	1.5
I-WP	7440	7391	0.7

Table 6. Comparison of first resonance frequency between the FEM and experimental test results of the FOGLG designed geometries.

Lattice type	FEM [Hz]	Experiment [Hz]	Relative error [%]
D	7440	7302	1.8
G	8510	8396	1.3
I-WP	7390	7358	0.4

1.3%, and 0.4% for the FOGLG designed D-, G-, and I-WP-type FGLs, respectively.

5. Conclusion

This study demonstrates the applicability of the HMTO and FOGLG methods to different TPMS lattice structures, namely, the D, G, and I-WP. As the first step, the effective stiffness values C_{11}, C_{12}, and C_{44} are compared to solid element-based lattice modeling to quantify the accuracy of the shell element-based lattice modeling. Even though the accuracy of the shell-element models decreases for the higher relative densities due to the shear and curvature effects, it is quite high at lower relative densities. Therefore, a case study of modal characterization of a sandwiched structure is conducted using the shell and solid models for the FOGLG and HMTO methods, respectively. Even though

© 2023 The Authors. Advanced Engineering Materials published by Wiley-VCH GmbH

15272648, 2023, 11, Downloaded from https://onlinelibrary.wiley.com/doi/10.1002/adem.202201811 by Ozyegin University, Wiley Online Library on [06/09/2023]. See the Terms and Conditions (https://onlinelibrary.wiley.com/terms-and-conditions) on Wiley Online Library for rules of use; OA articles are governed by the applicable Creative Commons License

there are some errors in the effective stiffness values of the shell models, using more shell elements in the FEM enables the FOGLG to attain a lower objective function compared to the HMTO. The optimal designs are then reconstructed using RDM and ERDM methods. The relative error in the first resonance frequency between the HMTO and reconstructed geometries using RDM is lower than 4% for all structures considered. The relative error between the FOGLG and the reconstructed geometries is further reduced by ERDM. The reconstructed geometries are then exported in the .stl format to fabricate the structure made from CoCr using the DMLM method. The quality of the fabricated FGLs is assessed and verified before experimental validation. Then, the structures designed by HMTO and FOGLG are validated by using a laser vibrometer. The results show that the reconstructed geometries by the RDM and ERDM methods perform a similar dynamic characteristic to the FEM with a relative error less than 2%. The contributions and conclusions of the study to the literature are summarized as follows: 1) Large-scale shell element-based lattice structures can be efficiently optimized with the FOGLG algorithm, for efficiently generating FGLs. 2) Both FOGLG and HMTO algorithms can be used to functionally grade a variety of surface-based lattices to improve the mechanical performance of the design domain, as validated by laser vibrometer testing. 3) The ERDM reconstruction algorithm is a strong candidate for the reconstruction of the shell element-based optimization.

The development of more accurate modeling methods for higher volume ratios is acknowledged as future work to design more efficient structures. Also, methods to reduce dust accumulation in enclosed regions are considered as important research topics.

Acknowledgements

This study was carried out under the TUBITAK Technology and Innovation Support Program (grant no.: 5158001).

Conflict of Interest

The authors declare no conflict of interest.

Data Availability Statement

The data that support the findings of this study are available from the corresponding author upon reasonable request.

Keywords

free-size optimization, functionally graded lattices, homogenization, topology optimization, triply periodic minimal surface (TPMS)

Received: December 14, 2022
Revised: February 22, 2023
Published online: March 21, 2023

[1] I. Maskery, A. Hussey, A. Panesar, A. Aremu, C. Tuck, I. Ashcroft, R. Hague, *J. Cell. Plast.* **2017**, *53*, 151.
[2] S. Yu, J. Sun, J. Bai, *Mater. Des.* **2019**, *182*, 108021.
[3] A. Dara, M. A. R. Bahubalendruni, A. J. Mertens, G. Balamurali, *Mater. Today Commun.* **2022**, *31*, 103286.
[4] A. Ghazlan, T. Nguyen, T. Ngo, S. Linforth, *Thin-Walled Struct.* **2020**, *151*, 106713.
[5] N. San Ha, G. Lu, *Compos. Part B Eng.* **2020**, *181*, 107496.
[6] X. Zheng, H. Lee, T. H. Weisgraber, M. Shusteff, J. DeOtte, E. B. Duoss, J. D. Kuntz, M. M. Biener, Q. Ge, J. A. Jackson, S. O. Kucheyev, N. X. Fang, C. M. Spadaccini, *Science* **2014**, *344*, 1373.
[7] M. Helou, S. Kara, *Int. J. Comput. Integr. Manuf.* **2018**, *31*, 243.
[8] M. Mahbod, M. Asgari, *Int. J. Mech. Sci.* **2019**, *155*, 248.
[9] S. Liang, L. Gao, Y. Zheng, H. Li, *Appl. Sci.* **2020**, *10*, 7449.
[10] S. Li, S. Zhao, W. Hou, C. Teng, Y. Hao, Y. Li, R. Yang, R. D. Misra, *Adv. Eng. Mater.* **2016**, *18*, 34.
[11] I. Maskery, A. O. Aremu, L. Parry, R. D. Wildman, C. J. Tuck, I. A. Ashcroft, *Mater. Des.* **2018**, *155*, 220.
[12] S. Daynes, S. Feih, W. F. Lu, J. Wei, *Mater. Des.* **2017**, *127*, 215.
[13] L. Li, G. Zhang, K. Khandelwal, *Int. J. Numer. Methods Eng.* **2017**, *112*, 737.
[14] G. I. Rozvany, M. Zhou, T. Birker, *Struct. Optim.* **1992**, *4*, 250.
[15] S. Watts, W. Arrighi, J. Kudo, D. A. Tortorelli, D. A. , *Struct. Multidiscip. Optim.* **2019**, *60*, 1887.
[16] Y. Agrawal, G. K. Ananthasuresh, *Struct. Multidiscip. Optim.* **2021**, *64*, 2489.
[17] M. Xiao, X. Liu, Y. Zhang, L. Gao, J. Gao, S. Chu, *Comput. Methods Appl. Mech. Eng.* **2021**, *384*, 113949.
[18] J. Gao, Z. Luo, L. Xia, L. Gao, *Struct. Multidiscip. Optim.* **2019**, *60*, 2621.
[19] C. Liu, Z. Du, W. Zhang, Y. Zhu, X. Guo, *J. Appl. Mech.* **2017**, *84*, 081008.
[20] D. Li, W. Liao, N. Dai, G. Dong, Y. Tang, Y. M. Xie, *Comput.-Aided Des.* **2018**, *104*, 87.
[21] S. Rastegarzadeh, J. Wang, J. Huang, *Volume 2: 42nd Computers and Information in Engineering Conf. (CIE)*, American Society of Mechanical Engineers, St. Louis, Missouri, USA August 14–17 **2022**, p. V002T02A041, https://doi.org/10.1115/DETC2022-89538/.
[22] M. P. Bendsøe, N. Kikuchi, *Comput. Methods Appl. Mech. Eng.* **1988**, *71*, 197.
[23] J. P. Groen, O. Sigmund, *Int. J. Numer. Methods Eng.* **2018**, *113*, 1148.
[24] U. Simsek, C. E. Gayir, G. Kiziltas, P. Sendur, *Int. J. Adv. Manuf. Technol.* **2020**, *111*, 1361.
[25] U. Simsek, A. Akbulut, C. E. Gayir, C. Basaran, P. Sendur, *Int. J. Adv. Manuf. Technol.* **2021**, *115*, 657.
[26] X. Chen, Q. Ji, J. Wei, H. Tan, J. Yu, P. Zhang, V. Laude, M. Kadic, *Int. J. Mech. Sci.* **2020**, *169*, 105288.
[27] N. Strömberg, *Volume 3A: 47th Design Automation Conf. (DAC)*, ASME, Virtual, Online, August 17–19 **2021**, p. V03AT03A029, https://doi.org/10.1115/DETC2021-67163.
[28] H. Jia, H. Lei, P. Wang, J. Meng, C. Li, H. Zhou, X. Zhang, D. Fang, *Extreme Mech. Lett.* **2020**, *37*, 100671.
[29] A. Kaveh, S. Talatahari, *Comput. Struct.* **2009**, *87*, 1129.
[30] J. Leiva, *10th AIAA/ISSMO Multidisciplinary Analysis and Optimization Conf.*, Albany, NY, 30 August **2004**, p. 4595.
[31] X. Han, W. An, A. Tovar, *Struct. Multidiscip. Optim.* **2019**, *59*, 2303.
[32] W. An, S. Wang, X. Han, *AIAA J.* **2021**, *59*, 4754.
[33] M. Tang, K. Lindkvist, *Master's Thesis*, Department of Design Sciences Faculty of Engineering LTH, Lund University, Lund, Sweden **2021**.
[34] U. Simsek, M. Ozdemir, P. Sendur, *Mater. Des.* **2021**, *210*, 110039.
[35] D. Li, N. Dai, Y. Tang, G. Dong, Y. F. Zhao, *J. Mech. Des.* **2019**, *141*, 071402.
[36] L. Zhang, B. Song, J. Fu, S. Wei, L. Yang, C. Yan, H. Li, L. Gao, Y. Shi, *J. Manuf. Processes* **2020**, *56*, 1166.
[37] H. Niknam, A. H. Akbarzadeh, *Mater. Des.* **2020**, *196*, 109129.

© 2023 The Authors. Advanced Engineering Materials published by Wiley-VCH GmbH

15272648, 2023, 11, Downloaded from https://onlinelibrary.wiley.com/doi/10.1002/adem.202201811 by Ozyegin University, Wiley Online Library on [06/09/2023]. See the Terms and Conditions (https://onlinelibrary.wiley.com/terms-and-conditions) on Wiley Online Library for rules of use; OA articles are governed by the applicable Creative Commons License

[38] L. J. Gibson, *MRS Bull.* **2003**, *28*, 270.
[39] L. Gibson, M. Ashby, in *Cellular Solids: Structure and Properties*, Cambridge Solid State Science Series, Cambridge University Press, Cambridge **1997**, pp. 309–344, https://doi.org/10.1017/CBO9781139878326.010.
[40] C. Yang, Q. M. Li, *Mech. Mater.* **2020**, *148*, 103536.
[41] Z. Xiao, Y. Yang, R. Xiao, Y. Bai, C. Song, D. Wang, *Mater. Des.* **2018**, *143*, 27.
[42] Z. Alomar, F. Concli, *Adv. Eng. Mater.* **2020**, *22*, 2000611.
[43] V. S. Deshpande, M. F. Ashby, N. A. Fleck, *Acta Mater.* **2001**, *49*, 1035.
[44] A. Bragov, A. Konstantinov, A. Lomunov, I. Sergeichev, B. Fedulov, *J. Phys. IV* **2009**, *137*, 1465.
[45] T. Maconachie, M. Leary, B. Lozanovski, X. Zhang, M. Qian, O. Faruque, M. Brandt, *Mater. Des.* **2019**, *183*, 108137.
[46] Y. Xu, D. Zhang, S. Hu, R. Chen, Y. Gu, X. Kong, J. Tao, Y. Jiang, *J. Mech. Behav. Biomed. Mater.* **2019**, *99*, 225.
[47] A. Panesar, M. Abdi, D. Hickman, I. Ashcroft, *Addit. Manuf.* **2018**, *19*, 81.
[48] O. Al-Ketan, R. K. Abu Al-Rub, *Mater. Des. Process. Commun.* **2021**, *3*, e205.
[49] N. Kladovasilakis, P. Charalampous, K. Tsongas, I. Kostavelis, D. Tzetzis, D. Tzovaras, *J. Manuf. Mater. Process.* **2021**, *5*, 95.
[50] J. H. Hong, F. Y. Yeoh, *Mater. Today Proc.* **2020**, *29*, 196.
[51] H. F. Morris, *J. Prosthet. Dent.* **1990**, *63*, 426.
[52] Online Materials Information Resource - MatWeb, MatWeb, L. L. C., https://www.matweb.com/ (accessed: February 2022).
[53] I. Maskery, L. Sturm, A. Aremu, A. Panesar, C. Williams, C. Tuck, R. Wildman, I. Ashcroft, R. Hague, *Polymer* **2018**, *152*, 62.
[54] D. Li, W. Liao, N. Dai, Y. M. Xie, *Comput.-Aided Des.* **2020**, *119*, 102787.
[55] G. Steven, *Eng. Comput.* **2006**, *23*, 432.
[56] G. P. Steven, *Commun. Numer. Methods Eng.* **1997**, *13*, 517.
[57] S. Xu, J. Shen, S. Zhou, X. Huang, Y. M. Xie, *Mater. Des.* **2016**, *93*, 443.
[58] Y. M. Xie, Z. H. Zuo, X. Huang, X. Yang, *J. Mech. Mater. Struct.* **2013**, *8*, 341.
[59] T. S. Newman, H. Yi, *Comput. Graphics* **2006**, *30*, 854.
[60] M. Alzahrani, S. K. Choi, D. W. Rosen, *Mater. Des.* **2015**, *85*, 349.
[61] Murata Manufacturing, Piezoelectric Ceramics (PIEZOTITE) Sensors, https://www.murata.com/ (accessed: April 2022).
[62] Polytec GmbH, Polytec OFV-5000 Vibrometer Controller, http://www.polytec.com/ (accessed: April 2022).

© 2023 The Authors. Advanced Engineering Materials published by Wiley-VCH GmbH

15272648, 2023, 11, Downloaded from https://onlinelibrary.wiley.com/doi/10.1002/adem.202201811 by Ozyegin University, Wiley Online Library on [06/09/2023]. See the Terms and Conditions (https://onlinelibrary.wiley.com/terms-and-conditions) on Wiley Online Library for rules of use; OA articles are governed by the applicable Creative Commons License